

## Analysis of Cu(In,Ga)Se<sub>2</sub> thin-film modules by electro-modulated luminescence

Vito Huhn, Andreas Gerber, Yael Augarten, Bart Elger Pieters, and Uwe Rau

Citation: *Journal of Applied Physics* **119**, 095704 (2016); doi: 10.1063/1.4942654

View online: <http://dx.doi.org/10.1063/1.4942654>

View Table of Contents: <http://scitation.aip.org/content/aip/journal/jap/119/9?ver=pdfcov>

Published by the [AIP Publishing](#)

---

### Articles you may be interested in

[A comparative study on charge carrier recombination across the junction region of Cu<sub>2</sub>ZnSn\(S,Se\)<sub>4</sub> and Cu\(In,Ga\)Se<sub>2</sub> thin film solar cells](#)

*AIP Advances* **6**, 035216 (2016); 10.1063/1.4944911

[Influence of different sulfur to selenium ratios on the structural and electronic properties of Cu\(In,Ga\)\(S,Se\)<sub>2</sub> thin films and solar cells formed by the stacked elemental layer process](#)

*J. Appl. Phys.* **116**, 174503 (2014); 10.1063/1.4900991

[The impact of oxygen incorporation during intrinsic ZnO sputtering on the performance of Cu\(In,Ga\)Se<sub>2</sub> thin film solar cells](#)

*Appl. Phys. Lett.* **105**, 083906 (2014); 10.1063/1.4894214

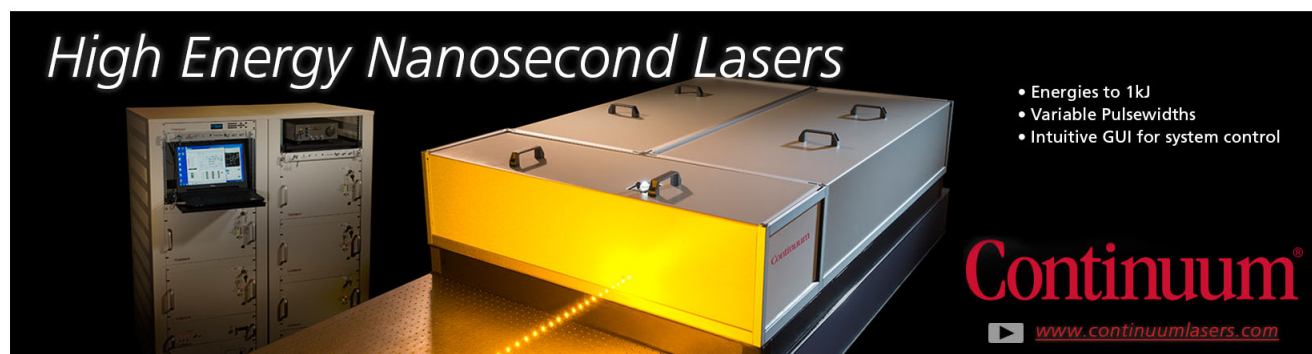
[Effect of light soaking on the electro- and photoluminescence of Cu\(In,Ga\)Se<sub>2</sub> solar cells](#)

*Appl. Phys. Lett.* **103**, 183504 (2013); 10.1063/1.4827260

[Microscale solar cells for high concentration on polycrystalline Cu\(In,Ga\)Se<sub>2</sub> thin films](#)

*Appl. Phys. Lett.* **98**, 264102 (2011); 10.1063/1.3604789

---

The advertisement features a large, industrial-grade laser system with a prominent yellow light output. To the left, a control rack with multiple modules and a monitor is visible. The background is dark, making the laser and its components stand out. The text 'High Energy Nanosecond Lasers' is written in a large, white, serif font at the top left. On the right, a list of features is provided: 'Energies to 1kJ', 'Variable Pulsewidths', and 'Intuitive GUI for system control'. The Continuum logo is displayed in a large, red, serif font at the bottom right, with the website 'www.continuumlasers.com' below it.

*High Energy Nanosecond Lasers*

- Energies to 1kJ
- Variable Pulsewidths
- Intuitive GUI for system control

**Continuum**<sup>®</sup>

[www.continuumlasers.com](http://www.continuumlasers.com)

# Analysis of Cu(In,Ga)Se<sub>2</sub> thin-film modules by electro-modulated luminescence

Vito Huhn,<sup>a)</sup> Andreas Gerber, Yael Augarten, Bart Elger Pieters, and Uwe Rau  
*IEK5-Photovoltaik, Forschungszentrum Jülich, 52425 Jülich, Germany*

(Received 11 December 2015; accepted 11 February 2016; published online 2 March 2016)

Thin-film Cu(In,Ga)Se<sub>2</sub> modules are investigated by electro-modulated luminescence with bias illumination. The large signal analysis enables the determination of the average current density/voltage ( $J/V$ ) characteristics of individual cell-strips in a module, without contacting each individual cell. It was found that the characteristics determined from electro-modulated photo-luminescence measurements differ from the characteristics determined without bias illumination via electro-luminescence. As a reason for this, we found the non-linear relation of the local current to the local voltage which makes the determination of the cell voltage via an average of the local voltages determined from electro-luminescence images incorrect especially at high injection currents. A second analysis method using the small signal response of electro-modulated photo-luminescence was also analyzed. Recently, a method based on such a small signal analysis was demonstrated that yields the local photocurrent collection efficiency. This contribution presents the first application of this method to solar modules with series connected cells rather than the previously shown analysis of single cells. We compare two ways to evaluate the photocurrent collection efficiency from the small signal analysis and discuss how applicable these measurements are to modules. We find that the photocurrent collection efficiency of modules gives valuable information about how defective cells act within a module and which parts of the module limit the overall current through the module. © 2016 AIP Publishing LLC. [<http://dx.doi.org/10.1063/1.4942654>]

## I. INTRODUCTION

Electro-luminescence (EL) and photo-luminescence (PL) imaging techniques are widely used to characterize solar cells.<sup>1–3</sup> Luminescence measurements methods offer fast, spatially resolved qualitative and quantitative information about defects and detrimental resistances in solar cells and modules. It has been shown that these methods are also applicable to thin-film technologies and were already used frequently to analyze Cu(In,Ga)Se<sub>2</sub> (CIGS) solar cells.<sup>4–10</sup> Luminescence methods are especially valuable if used close to the real working conditions of the photovoltaic devices, i.e., under illumination and close to the maximum power point.

In the present paper, we analyze electro-luminescence and electro-modulated photo-luminescence (EM-PL, i.e., luminescence under modulated external voltage and constant light bias) measurements of CIGS mini-modules to characterize individual cells in a module under relevant working conditions. The work here is divided into two major parts: the large-signal and the small-signal analysis.

The large-signal analysis uses voltage dependent luminescence images at a given bias/working point. It has already been shown that the large-signal analysis of EL measurements can be used to analyze power losses in a module.<sup>4</sup> In this work, we add a large-signal analysis of EM-PL measurements and compare it with EL measurements. The reciprocity theorem states that both methods should be equally

usable, but it was also seen that there are differences between the EL and EM-PL emission under high injection conditions.<sup>11</sup> This possibly introduces also a difference in the large signal analysis done under illumination compared to measurements in the dark, which influences the quantitative interpretation of the results, as it might not be appropriate to use measurements in the dark to describe the performance of cells under illumination.

The second part of this work focuses on the small-signal analysis. Here, we measure the differential change of the photo-luminescence image with the externally applied voltage. With the small-signal images, we determine the photocurrent collection efficiency of the analyzed modules. The photocurrent collection efficiency provides quantitative information about resistive and recombination effects<sup>12,13</sup> and has already been successfully demonstrated using multicrystalline solar cells.<sup>14</sup> We compare different calculation methods and discuss how applicable this method is for solar modules, taking into account that the cells in a module are connected in series.

## II. LARGE-SIGNAL ANALYSIS

### A. Theory

The relation between the EL emission and the junction voltage of a solar cell is described by the reciprocity theorem.<sup>15</sup> It has been shown that this theorem can also be applied to describe the EM-PL emission  $\Phi_{EM-PL}$  of solar cells.<sup>16</sup> This relation has already been shown to be applicable to CIGS solar cells.<sup>11</sup> For a given photon energy  $E$ , and sample position  $r$ , the reciprocity theorem reads

<sup>a)</sup>Author to whom correspondence should be addressed. Electronic mail: v.huhn@fz-juelich.de. Phone: +49 2461 61-4855.

$$\Phi_{EM-PL}(E, \mathbf{r}, V_{ext}) = \Phi_{SC}(E, \mathbf{r}, \Phi_{exc}) + Q_e(E, \mathbf{r})\Phi_{bb}(E) \times \left[ \exp\left(\frac{V_j(\mathbf{r}, V_{ext})}{V_{th}}\right) - 1 \right], \quad (1)$$

where  $\Phi_{bb}(E)$  is the black body spectrum,  $Q_e(E, \mathbf{r})$  the external quantum efficiency, and  $V_j(\mathbf{r}, V_{ext})$  the local junction voltage.  $V_{th}$  is the thermal voltage. The quantity  $V_{ext}$  denotes the external voltage applied to the terminals of the device. The voltage independent term  $\Phi_{SC}(E, \mathbf{r}, \Phi_{exc})$  is the luminescence emitted from the sample at short circuit, with a photo-excitation  $\Phi_{exc}$ . The camera signal  $S_{cam}(\mathbf{r}, V_{ext})$  from the position  $\mathbf{r}$  on the sample is equal to

$$S_{cam}(\mathbf{r}, V_{ext}) = \int Q_{cam}(E)\Phi_{EM-PL}(E, \mathbf{r}, V_{ext})dE. \quad (2)$$

Here,  $Q_{cam}$  is the sensitivity (EQE) of the charge coupled device camera that is used to image the sample.<sup>4,17</sup> Combination of Eq. (2) with Eq. (1) yields

$$\begin{aligned} S_{cam}(\mathbf{r}, V_{ext}) &= \int Q_{cam}(E)\Phi_{SC}(E, \mathbf{r}, \Phi_{exc})dE \\ &+ \int Q_{cam}(E)Q_e(E, \mathbf{r})\Phi_{bb}(E)dE \\ &\times \left[ \exp\left(\frac{V_j(\mathbf{r}, V_{ext})}{V_{th}}\right) - 1 \right] \\ &= S_{SC}(\mathbf{r}) + S_0(\mathbf{r}) \left[ \exp\left(\frac{V_j(\mathbf{r}, V_{ext})}{V_{th}}\right) - 1 \right]. \end{aligned} \quad (3)$$

In Eq. (3), the short circuit signal  $S_{SC}(\mathbf{r})$  may also contain spurious reflections from the excitation light.<sup>18,19</sup> The saturation signal  $S_0(\mathbf{r})$  via its dependence on the external quantum efficiency reflects the local recombination as well as local optical properties.<sup>20</sup>

In order to relate the camera signal at a certain external voltage to a local junction voltage, we first need to remove the voltage independent short circuit signal  $S_{SC}(\mathbf{r})$ . This is done by subtracting an image taken under short circuit conditions from an image taken with the sample at the required external bias yielding the large signal difference

$$\begin{aligned} \Delta S_{EM-PL}(\mathbf{r}, V_{ext}) &= S_{cam}(\mathbf{r}, V_{ext}) - S_{cam}(\mathbf{r}, V_{ext} = 0) \\ &= S_0(\mathbf{r}) \exp\left(\frac{V_j(\mathbf{r}, V_{ext})}{V_{th}}\right). \end{aligned} \quad (4)$$

Note the second equality in Eq. (4) assumes  $V_j(\mathbf{r}, V_{ext} = 0) = 0$ . From Eq. (4) follows

$$\begin{aligned} \Delta V_j(\mathbf{r}, V_{ext}) &:= V_{th} \ln(\Delta S_{EM-PL}(\mathbf{r}, V_{ext})) \\ &= V_j(\mathbf{r}, V_{ext}) - V_{th} \ln(S_0) = V_j(\mathbf{r}, V_{ext}) + C, \end{aligned} \quad (5)$$

where  $\Delta V_j$  is the information we get directly from luminescence images, without any further information. The quantity  $\Delta V_j$  has the unit of a voltage but describes the real local junction voltages only modulo the voltage offset  $C$ , where  $C$  is independent of the applied voltage. In the following,  $C$  is assumed to be the same at different coordinates  $\mathbf{r}$ , implying a constant quantum efficiency and temperature over the

entire module area. In this situation, the local junction voltage variations  $V_j(\mathbf{r}, V_{ext})$  are essentially determined by shunts and series resistances.<sup>4</sup>

We use a method described by Glatthaar *et al.*<sup>21</sup> for cells and applied by Helbig *et al.*<sup>4</sup> to modules to determine  $C$ : It holds that  $V_{ext}$  is equal to the sum of the local junction voltage of each cell in the module plus an additional voltage drop across all the series resistances in the module. The voltage across the series resistances is unknown. However, under open circuit conditions the voltage drop across the series resistance is zero. Thus, we can determine  $C$  with EM-PL measurements using Equation (6), with the module at open circuit. The voltage drop across each cell is assumed to be equal to the average local junction voltage of each cell. That is to say,

$$\sum_{i=1}^n \bar{V}_i(J=0) = V_{oc}, \quad (6)$$

where  $\bar{V}_i(J=0)$  denotes the average junction voltage of cell  $i$  when the module is at open circuit and  $n$  is the number of cells in the module. With this relation, and Equation (5) the scaling factor  $C$  can be calculated for the module using

$$C = \frac{\sum_{i=1}^n \bar{\Delta V}_i - V_{oc}}{n}, \quad (7)$$

where  $\bar{\Delta V}_i$  is the mean of  $\Delta V_j(\mathbf{r}, V_{ext})$  determined via Eq. (5) from the EM-PL image taken under open circuit conditions for cell  $i$ . For the determination of  $C$  from EL images, Equation (7) can be used in a similar way. In this case, however,  $\bar{\Delta V}_i$  is determined via Eq. (5) using EL images taken, while the injected current is equal to the short circuit current  $J_{sc}$  which corresponds to the  $V_{oc}$  used. This ensures that the local junction voltage of the diode is equal to its known open circuit voltage, although a higher external voltage is applied, because the same amount of current is pushed through the junction as is injected under open circuit conditions.

As now, the local voltages of each cell in the module can be calculated using Equations (5) and (7), a  $J/V$  curve can be established for each cell in the module by taking the average local junction voltage as the voltage across each cell at known injected currents.<sup>4</sup> Note that this method gives a  $J/V$  characteristic of the junction properties of each cell, as only the voltage drop across the junction is measurable. The  $J/V$  characteristic determined from EL and EM-PL measurements does not include information about series resistance and therefore more closely resemble  $J_{sc}/V_{oc}$  characteristics.  $J_{sc}/V_{oc}$  measurements relate  $V_{oc}$  to  $J_{sc}$  at varying illuminations, and give a sample  $J/V$  curve without the influence of series resistance.<sup>22</sup> Additionally, for this method to work we assume that the average junction voltage of each cell can be used as the correct cell voltage. We will discuss in detail in Section II C how viable this assumption is.

## B. Experimental results

For the experiments performed in this work, we used two industrially produced  $8.6 \text{ cm} \times 7 \text{ cm}$  CIGS mini-modules with 17 cells from the company MANZ. One showed a few



defects (shunts), while the other one did not show any obvious defects. They were contacted via contact pins at the outer cells. A four point measurement setup was used to minimize the influence of the contact resistance. The sample was held at a constant temperature of 25 °C during all the measurements via Peltier elements and water cooling. The luminescence images were taken with a Princeton Instruments Nirvana640 InGaAs camera (640 × 512 pixels) cooled to −80 °C. For the EM-PL images, the sample was held under constant illumination using a 90 W, 808 nm diode laser, with an intensity of 1 sun equivalent. Luminescence images were taken at 0.1 V steps between short circuit current and open circuit voltage to obtain a full  $J/V$ -characteristic.

Figs. 1 and 2 show EL and EM-PL images of the two samples taken with a terminal voltage of 0.68 V/cell, close to the  $V_{oc}$  of the samples. Background corrections via the subtraction of dark images for the EL images and the subtraction of an image taken under short circuit conditions for the EM-PL images were made. Sample two (Fig. 2) clearly shows 4 defects (shunts) with varying strength, while sample one in Fig. 1 does not show any defects. The intensity variations of the first cell on the left result from the contacting method, as the pins used for contacting are directly placed on the TCO left of the left cell, which leads to more luminescence intensity close to the pins, due to a higher local current flow close to the contact pins. This effect is less prominent on the right

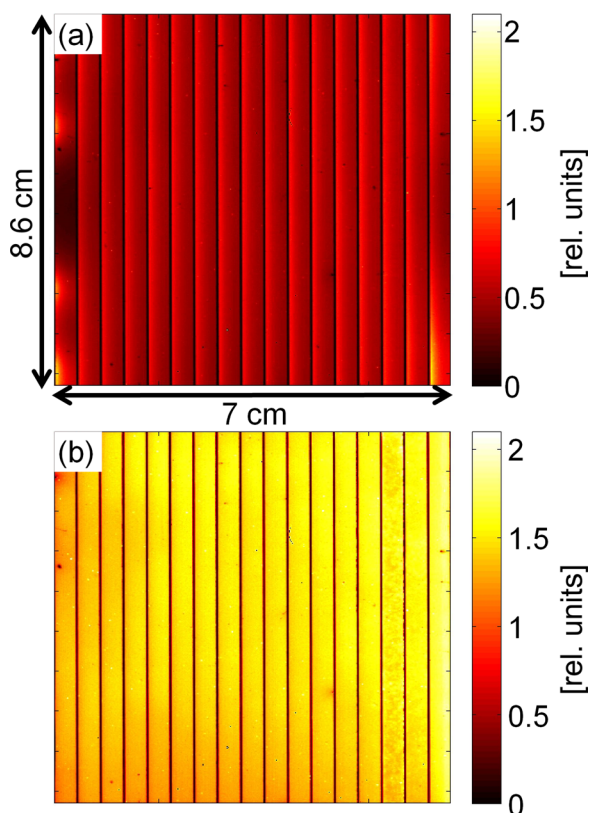


FIG. 1. (a) EL image of the analyzed CIGS mini-module without severe defects (sample 1) with a terminal voltage of 0.68 V/cell. (b) EM-PL images of the same module under 1 sun illumination with a terminal voltage of 0.68 V/cell. The EM-PL images shows a higher intensity as at the same voltage more current is injected, while in the EL image the injected current is reduced by series resistance.

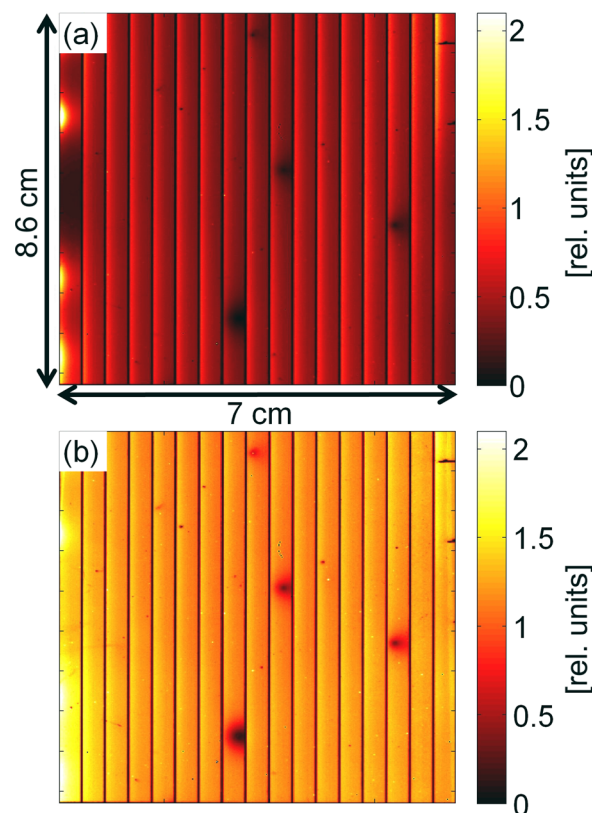


FIG. 2. (a) EL image of the analyzed CIGS mini-module with defects (sample 2) and an externally applied voltage of 0.68 V/cell. (b) EM-PL images of the same module under 1 sun illumination with a terminal voltage of 0.68 V/cell. Both images clearly show shunts (dark spots) in the 8th, 9th, 10th, and 15th cell from the left.

side of the module due to the lower sheet resistance of the molybdenum.

We use Equations (5) and (7) to determine the local voltages. To determine  $C$ , we used the PL images taken under open circuit conditions and related them to the open circuit voltage. This method seemed more reliable in our case as EL images under low injection conditions are always subject to low signal-to-noise ratios, while for EL images at higher injection conditions the mean junction voltage might not relate to the overall cell voltage (Section II C). The same  $C$  determined from the open circuit PL image is then used for the determination of the  $J/V$  characteristics of the individual cells in the module from the EL images. As the cells are series connected, the current through each cell is the same and equal to the externally measured module current, while the voltage of the individual cells is determined from the mean of the local junction voltages of each cell. Fig. 3 shows a standard  $J/V$  characteristic (blue), a  $J_{sc}/V_{oc}$  characteristic (light blue) and the two characteristics determined from the EL and EM-PL images (black and red, respectively). The characteristic from the images for the whole module is determined by adding up the calculated voltages of the individual cells. As visible in Fig. 3, the characteristics determined from the images are similar to the  $J_{sc}/V_{oc}$  characteristic of the module (note that  $C$  was determined such that the EM-PL characteristic matches the  $J/V$  characteristic at the open circuit voltage). Still, we see differences between the EL and

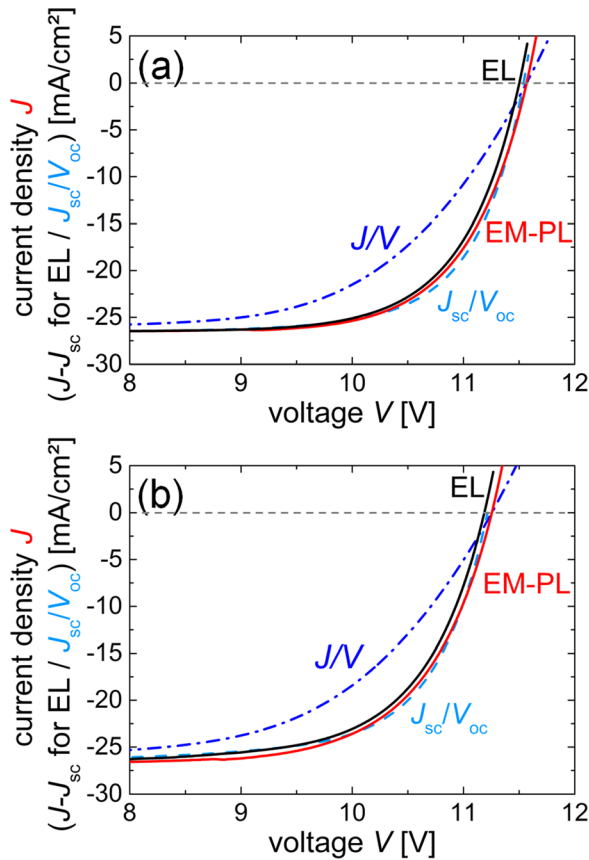


FIG. 3. Comparison of a standard measured  $J/V$  characteristic (blue, dashed dotted), a  $J_{sc}/V_{oc}$  characteristic (light blue, dashed), and characteristics reconstructed from the EL (black, solid) and EM-PL (red, solid) measurements. (a) Module with no severe defect, (b) module with shunted cells. The EL and  $J_{sc}/V_{oc}$  characteristics were shifted down by the short circuit current density.

the EM-PL characteristics for the good and the defected module which cannot be explained easily as the reciprocity theorem would suggest the same results from EL and EM-PL characteristics due to the superposition (Equation (1)). The EL characteristics of both modules show at higher injected currents lower voltages than the EM-PL characteristic determined under illumination. The defected module also shows a difference between the EL and EM-PL characteristic at lower injected currents.

Fig. 4 shows  $J/V$  characteristics determined for an individual shunted cell (dashed curve) and a non-shunted cell (solid curve) in the defected module (sample 2). We clearly see in the EL as well as in the EM-PL characteristics that the voltages across the shunted cells are reduced. However, we see again the difference between the characteristics from EL and EM-PL images, as the influence of the shunt seems much less in the EM-PL characteristic especially at lower voltages and the EM-PL characteristics show in general higher voltages. The results will be discussed in Section II C.

### C. Discussion and simulation

Based on the reciprocity theorem, the  $J/V$  characteristics calculated from EL and EM-PL images should be equal, as (by the superposition principle) Equations (4) and (5) are valid for the dark as well as the illuminated case. It is

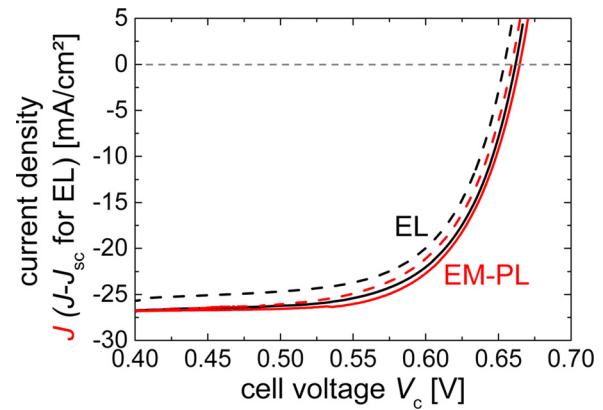


FIG. 4. Cell characteristics determined from EL and EM-PL images (black and red, respectively). The dashed lines show the characteristic of a shunted cell in the defected module (cell 8 from the left) while the solid lines are determined for a cell without defects in the same module (cell 5 from the left). The EL curves were shifted down by  $J_{sc}$ , for easier comparison.

unlikely that the constant  $C$  is different for the illuminated and dark case. The temperature of the sample was held at 25 °C in all cases, and we do not expect the quantum efficiency of the sample to be illumination dependent. One explanation may be that the different potential distributions within the cells under EL as compared to EM-PL lead to a difference in the local junction voltage mean at the same injected current. The assumption that the mean of the local voltages is equal to the overall cell voltage only holds if the voltage variations over the cell are small enough to approximate the diode as linear. For example, if one wants to determine the cell voltage from an EL image under high injection conditions, one introduces an error when one uses the mean of the local voltages within this cell. The sheet resistance leads under high injection conditions to a larger variation of the local junction voltage as it will be larger on one side of the cell than on the other (Figs. 1(a) and 6(a)). Due to the exponential dependence of the current on the local voltage, the higher local voltages are more important for the overall cell voltage drop than the lower local junction voltages, as the regions with higher voltages carry more current. If one takes a simple mean of the local voltage to determine the cell voltage, one underestimates the high voltages, which results in a cell voltage which is determined to low. For the same reason, we use the EM-PL images to calibrate our luminescence intensities to real voltages. At open circuit conditions the local voltages do not vary across the cell as no current flows in the module, and therefore the series resistance has no influence on the local voltage distribution and the mean of the local junction voltage becomes a reliable value for the actual voltage across the cell (Fig. 6(b)). This explains why the EL characteristics show lower voltages as the EM-PL and  $J_{sc}/V_{oc}$  characteristic at higher injected currents.

To further investigate if the difference of EL, EM-PL, and  $J_{sc}/V_{oc}$  mainly results from the error introduced by taking the mean of the local junction voltages of one cell as an estimate of the true cell voltage, we used simulations. For the simulations, the program PVMOS was used.<sup>23</sup> The open source PVMOS program can simulate local voltage distributions within a solar module by solving the governing

differential equations using the network simulation method. It features a variable and adaptive mesh and flexible meshing tools allowing the simulation of both crystalline silicon as well as thin-film technologies. Through the simulation it is possible to directly determine the local junction voltages of shunted and non-shunted cells in a module under arbitrary conditions, which removes any error introduced by the calculation of the proportionality constant  $C$ . Additionally, it is possible to extract a  $J_{sc}/V_{oc}$  characteristic for every cell in the module, which makes it possible to see the error that results from taking the mean as the real voltage estimate. We simulated both the good and defected modules. The input data for the simulations were calibrated to the experimentally measured data. The module and individual cell size and geometry were chosen to match the real samples. The p-n-junction was approximated with a one-diode model. The short circuit current densities and the recombination current were adjusted so that the simulated  $J_{sc}$  and  $V_{oc}$  matched the experimentally measured values. A TCO sheet resistance of  $24 \Omega/sq$  and a back contact sheet resistance of  $0.8 \Omega/sq$  were used. Using these parameters, the p2 resistance and internal series resistance were then adjusted so that the simulated and measured  $J/V$  characteristics of the modules matched. For the module with defects, we introduced four ohmic shunts into the module at the same positions as they were in the original sample. Their strength and size were adjusted so that a simulated local voltages image under illumination at open circuit matched the PL measurement. The result can be seen in Fig. 5. Note that

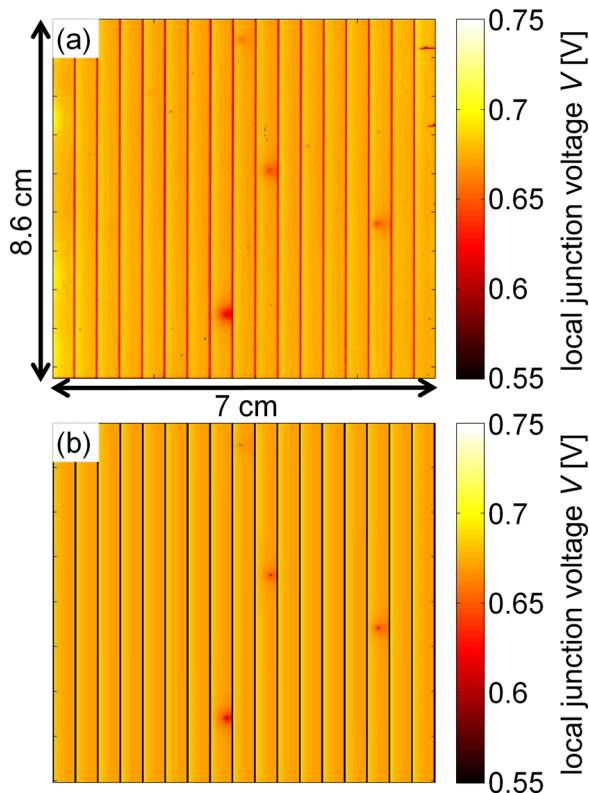


FIG. 5. (a) Local junction voltages determined from an EM-PL image at  $V_{ext} = 11.8$  V. (b) Local junction voltages determined for the simulated module at  $V_{ext} = 11.8$  V.

we did not perform extensive fitting procedures and some differences exist between the simulated and real devices. However, it is a model with reasonable parameters and should therefore be useful to understand our results. Fig. 6 shows a line scans of the local voltage of a non-shunted cell in the module in the dark (6(a)) and in the light (6(b)) at the same amount of injected current (dark:  $J = 27 \text{ mA/cm}^2$ ; light:  $J - J_{sc} = 27 \text{ mA/cm}^2$ ). It is clearly visible how the different injection conditions lead to different distributions of the local voltages. Although in both cases the overall recombination current in the cells is the same and therefore the corresponding voltage drop across the cell should also be the same, we see that using the mean of the local junction voltage does not yield the desired result. In the EL case, the cell voltage is underestimated due to the larger current flow in the regions of higher voltages, while in the EM-PL case the result is more reliable as the line scan was determined while the sample was close to open circuit conditions.

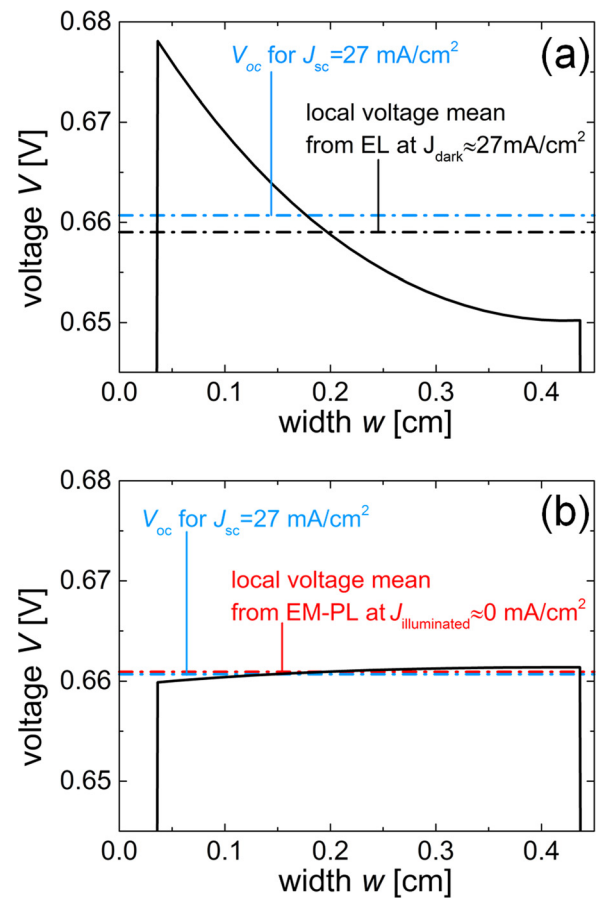


FIG. 6. Comparison of line scans of the local voltages simulated in the dark (a) and under illumination (b) with the same amount of charge carrier recombination ( $27 \text{ mA/cm}^2$ ). (a) If the charge carriers are electrically injected there is a larger variation of the local voltages across the cell and as the local current depends exponentially on the local voltage the local voltage mean underestimates the real voltage drop across the cell (determined from  $V_{oc}$  when  $J_{sc} = 27 \text{ mA/cm}^2$ ). (b) If the charge carriers are injected via illumination the local voltage variation is reversed if the overall current is negative but also in this case a lot smaller as the recombination current is close  $J_{sc}$  and the net current flow is close to zero. Thus, the mean of the local junction voltage determined via EM-PL measurements is a more reliable value for the voltage drop across the cell close to open circuit conditions.



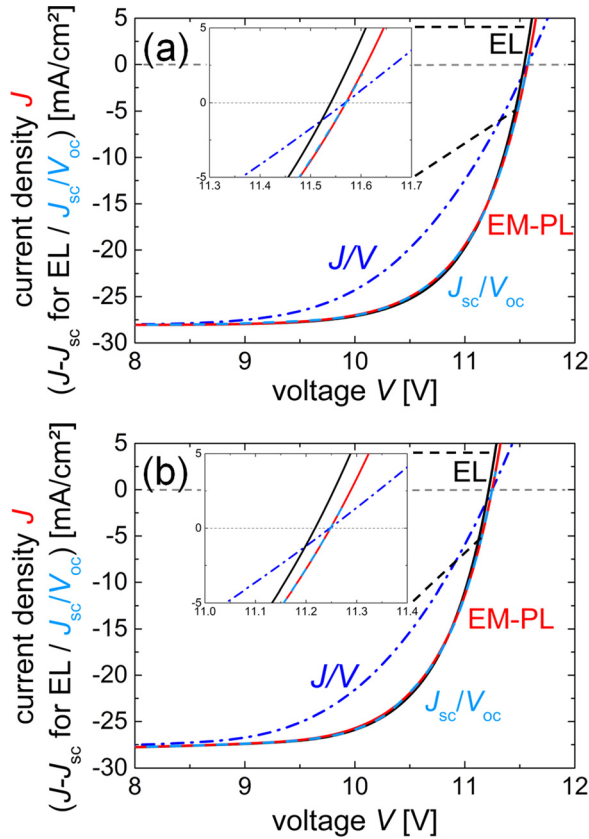


FIG. 7. Comparison of simulated characteristics:  $J/V$  (blue, dashed dotted),  $J_{sc}/V_{oc}$  (light blue, dashed), and characteristics reconstructed from the local voltages determined in the dark (black, solid) and illuminated (red, solid) cases. (a) Module with no severe defect, (b) Module with shunted cells. The  $J_{sc}/V_{oc}$  characteristics and the characteristic determined from the dark case have been shifted down by the short circuit current density (for ease of comparison). The inset shows how the dark (EL) characteristic differs from the EM-PL and  $J_{sc}/V_{oc}$  characteristics at larger voltages.

Fig. 7 shows additionally a simulated  $J/V$  and  $J_{sc}/V_{oc}$  characteristics, as well as the characteristics determined from the local junction voltages of the sample in the dark and under illuminated conditions (EL and EM-PL). These results are shown for both the good and defected simulations. The characteristics determined from the simulated local junction voltages are in both cases very similar to the module  $J_{sc}/V_{oc}$  characteristic, which implies the viability of the method. Note that this works equally well for the good module and the one with defects. We also see that the EL characteristic differs from  $J_{sc}/V_{oc}$  and EM-PL characteristics at higher voltages. Although this effect is less pronounced than in our measurements it shows that as predicted, for realistic samples, using the mean of the local voltages to determine the actual cell voltages does, indeed, introduce a visible error. This error depends on the current variations within one cell and therefore the sheet resistance and shunts, and also the internal series resistance of each cell stripe.

Simulated  $J/V$  characteristics of the individual cells determined from the local junction voltages were also compared to the  $J_{sc}/V_{oc}$  characteristic of the individual cells, which are accessible in the simulations. Fig. 8(a) shows these characteristics for a shunted and a non-shunted cell of the defected module. Similar to the experimental results, we

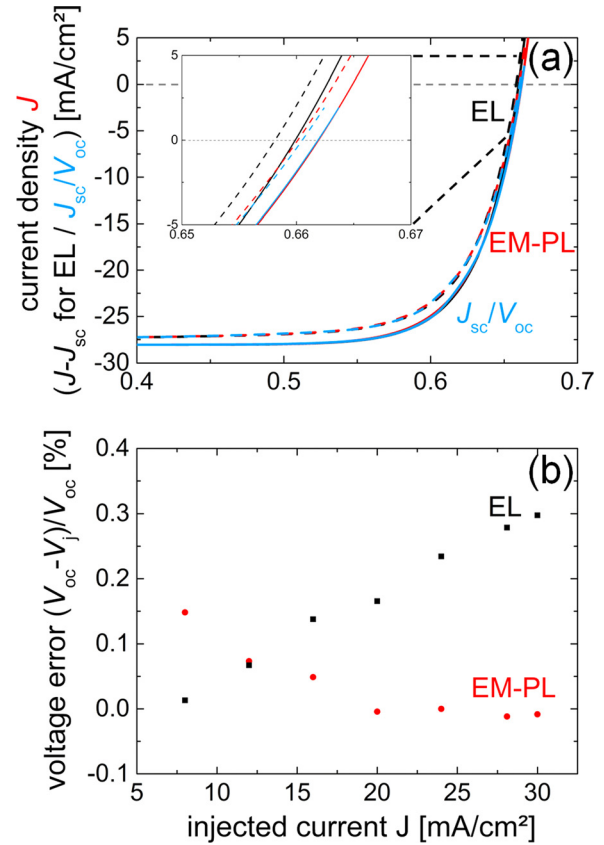


FIG. 8. (a) Simulated EL (black), EM-PL (red), and  $J_{sc}/V_{oc}$  (light blue) characteristics of cells within a simulated module. Solid lines: non-shunted cell. Dashed lines: shunted cell. (b) Difference in percent between the characteristics determined via luminescence and the  $J_{sc}/V_{oc}$  characteristic of a non-shunted cell.

clearly see the effect of the shunt in the reduced voltages of the characteristic for the shunted cell. The characteristics determined from the local voltages agree well with  $J_{sc}/V_{oc}$  characteristic, which implies that it is possible to calculate  $J/V$  characteristics of individual cells from luminescence images. However, these simulations were not able to reproduce the difference between the EL and EM-PL characteristics at low voltages that we saw in our measurements. One can think of several aspects which were not considered in the simulations which could lead to such a result. For example, act shunts in the laser lines differently under illumination and in the dark which could alter the measured local voltages and might not be clearly visible in the luminescence images. Also light trapping and reflections within the sample could play a role. Additional is the signal to noise ratio especially of the shunted cells at low applied voltages which might influence the results although an average of the local voltage is taken.

In summary, both the simulations and experiments show that it is possible to determine  $J/V$  characteristics of cells from luminescence imaging of modules. Both EL and EM-PL measurements can be used, but both methods show errors depending on the conditions and the properties of the module. As seen in Fig. 8(b), EL measurements underestimate the actual cell voltage at high injected current and are therefore less appropriate to determine cell characteristics under

these operating conditions. Thus, close to the open circuit voltage EM-PL measurements should be used to determine the actual cell voltages. However, EM-PL measurements are more likely to be erroneous at lower applied voltages. On the one hand, because the overall current through the module is larger and therefore the variations over the cell area in voltage and local current density become larger, leading to an underestimation of the actual cell voltage (Fig. 8(b)). On the other hand, because the real injected current through the diode can be different to the one assumed, as the measured short circuit current can be influenced by series and shunt resistances, and therefore shifting the measured current by this value introduces an additional error.

### III. SMALL-SIGNAL ANALYSIS

#### A. Theory

Wong and Green<sup>12</sup> described how small differences of the voltages extracted via luminescence measurements can be used to determine the so called photocurrent collection efficiency, also called current transport efficiency  $f_{PC}$ . The photocurrent collection efficiency is a measure of how efficiently additional created charge carrier are collected at the terminals of the sample. The quantity  $f_{PC}$  is described as the ratio between the change of locally generated photocurrent  $\delta I_L^r$  and the change of the resulting current through the complete cell  $\delta I_{ext}$ :

$$f_{PC}(\mathbf{r}, V_{ext}) := \left. \frac{\delta I_{ext}}{\delta I_L^r} \right|_{\delta V_{ext}=0} = \left. \frac{\delta V_j(\mathbf{r})}{\delta V_{ext}} \right|_{\delta I_L=0}. \quad (8)$$

The latter relation was derived by Wong and Green for a linearized representation of a solar cell network<sup>12</sup> and was extended in Ref. 24 for solar modules. It shows that  $f_{PC}$  is measureable by determining the change of the local junction voltage  $\delta V_j(\mathbf{r})$  caused by a differential change of the terminal voltage  $\delta V_{ext}$ .

It is important to note that  $f_{PC}$  is dependent on the chosen operating point. At higher voltages, the diode resistance is reduced compared to the series resistance. Charge carriers which are collected at the p-n junction will travel along the paths of least resistance. The higher the diode operating voltage, the likelier it is that charge carriers recombine across the diode instead of leaving the solar cell along the distributed series resistance and be collected at the terminals. Thus, a larger operating voltage results in a decreased photocurrent collection efficiency, and the rate at which the photocurrent collection efficiency decreases with the applied voltage mainly depends on the distributed series resistance.

There are two methods that can be used to determine  $f_{PC}$  from luminescence images. In the first method, suggested by Wong and Green, two EM-PL images are taken under the same illumination intensity, but at slightly different operating points. An image of the local junction voltage is then calculated from each of these two images, using Equation (5). The difference between the two voltage images gives an image of  $\delta V_j$ . Thus,  $f_{PC}$  can be calculated with Equation (8), with  $\delta V_{ext}$  being the difference of the two terminal voltages at which the two images were taken. From

now on, this method will be referred to as the log-method, since the logarithm of the EM-PL images has to be calculated.

The second method, derived in Ref. 12, instead uses a linear approximation of the  $J/V$  characteristic at the chosen operating point to calculate the photocurrent collection efficiency without the need for determining the local junction voltages first. The formula for this method is

$$f_{PC,approx}(\mathbf{r}, V_{ext}) = \frac{\delta S_{cam}}{\Delta S_{cam}} \frac{V_{th}}{\delta V_{ext}}, \quad (9)$$

where  $\delta S_{cam}$  is the difference between two luminescence images taken at  $V_{ext} \pm 1/2 \delta V_{ext}$ , and  $\Delta S_{cam}$  is the difference between images taken at the desired operating point  $V_{ext}$  and at short circuit. We call the method from now on the linear-method since it uses a linear approximation for the determination of the local voltage change. If we look into the second order of the approximation, we see that

$$f_{PC,approx} \approx f_{PC} \left( 1 + \frac{f_{PC}^2 \delta V_{ext}^2}{24 V_{th}^2} \right). \quad (10)$$

Thus, the approximation will always overestimate the photocurrent collection efficiency if  $\delta V_{ext}^2 / 24 V_{th}^2$  is not small compared to one ( $\delta V_{ext} \ll 0.13$  V at room temperature for a single cell). As  $f_{PC}$  is a differential value,  $\delta V_{ext}$  needs to be chosen small enough so that the operating point for the measured  $f_{PC}$  is well defined. However, if  $\delta V_{ext}$  is chosen too small,  $\delta V_j$  will no longer be measureable, as noise will dominate the difference image. Thus, choosing a larger  $\delta V_{ext}$  enhances the signal to noise ratio but it also introduces an error as the operating point is less well defined.

#### B. Experimental results

From the measured EM-PL images discussed in Section II B, it is an easy task to calculate photocurrent collection images. As an image was taken every 0.1 V, the photocurrent collection images can be calculated at any operating point using the two methods described in Sec. III A with  $\delta V_{ext} = 0.012$  V/cell. Fig. 9 shows photocurrent collection efficiency images of sample 2 calculated using the two different methods. All images are taken at an operating point of 0.56 V/cell, which is slightly higher than the maximum power point of the module. The  $\delta V_{ext}$  used is shown on each image. The images show photocurrent collection efficiencies between zero and approximately 0.06. For a single cell, one would expect current collection efficiencies between zero and one. For a module however, the photocurrent collection efficiency is in general reduced by an approximate factor of  $1/n$ , where  $n$  is the number of cells. Any external voltage applied drops across all the cells in the module and therefor is the local voltage change on each cell approximately reduced by  $1/n$  which, in turn, reduces the photocurrent collection efficiency. One can also explain this by looking at local illumination changes when the external voltage is kept constant. If the generation of charge carriers is changed in one spot of an individual cell in the module, it is clear that this whole change cannot be



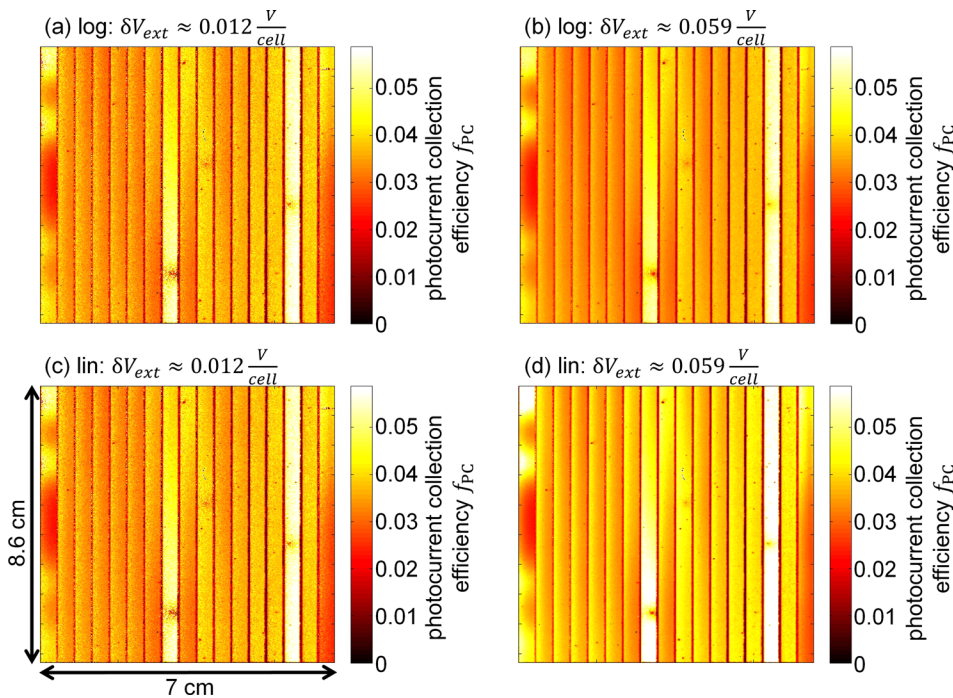


FIG. 9. Comparison of Photocurrent collection efficiency images of sample 2 at an operating point of 0.56 V/cell calculated with different formulas and different  $\delta V_{ext}$ . (a) and (b) Calculated using the log-Method and  $\delta V_{ext} = 0.012$  V/cell and 0.059 V/cell, respectively. (c) and (d) Calculated using the linear-Method and  $\delta V_{ext} = 0.012$  V/cell and 0.059 V/cell, respectively. At low  $\delta V_{ext}$  both methods yield the same results, but at higher  $\delta V_{ext}$  the change in the image calculated with the linear-method is larger, while the log-method shows very little change.

transferred to an external circuit as the current through each cell has to be the same. Thus, the series connection of the cells reduces the photocurrent collection efficiency of each cell.

The two methods to calculate  $f_{PC}$  are compared with respect to the choice of  $\delta V_{ext}$ . As the second method is a linear approximation both methods should yield the same result for small  $\delta V_{ext}$ , and deviate as  $\delta V_{ext}$  is increased. Fig. 9 shows the  $f_{PC}$  images determined with both methods and varying  $\delta V_{ext}$ . Images (a) and (b) are calculated using the log-method. Image (b) with the larger  $\delta V_{ext}$  gives a very similar result to image (a), except that it is less noisy. Images (c) and (d) are calculated using the linear-method. Image (d) demonstrates a higher  $f_{PC}$  than (c), showing that the calculated photocurrent collection efficiency increases if  $\delta V_{ext}$  is increased, when the linear-method is used, as expected.

To look at the dependency of the two methods on  $\delta V_{ext}$  in detail, Fig. 10 shows the mean of the photocurrent collection efficiency plotted versus the chosen  $\delta V_{ext}$ . At low  $\delta V_{ext}$ , both methods yield approximately the same results. We also clearly see that the linear-method overestimates the photocurrent collection efficiency if the  $\delta V_{ext}$  is chosen too large, as calculated in Equation (10). The  $\delta V_{ext}$  dependency of the photocurrent collection efficiency calculated via the log-method is significantly less and only shows a slight underestimation towards higher  $\delta V_{ext}$ . When  $\delta V_{ext}$  is increased from 0.013 V/cell to 0.063 V/cell, the average  $f_{PC}$  of the module calculated via the linear-method increases by 8.3%, while the average  $f_{PC}$  of the log-method decreases by only 1.6%.

The first cell on the left (Fig. 9) clearly shows the information we get from measuring the photocurrent collection efficiency. This cell shows brighter and less bright regions. As discussed earlier this results from the positioning of the contacting pins next to this cell on the TCO. Charge carriers generated close to these contacting pins have a higher probability of being collected. Additionally, we see that the shunted cells show a higher photocurrent collection

efficiency than the non-shunted cells. This result is somewhat non-intuitive and will be discussed in detail in Section III C.

In Fig. 11, the photocurrent collection efficiency measured at a higher operating point of 0.68 V/cell, which is slightly below  $V_{oc}$ , is shown. In this image, all the cells in the module look similar (the shunted cell is no longer much brighter) and the overall photocurrent collection efficiency is reduced due to the higher operating point. We can also see a very clear horizontal gradient in the photocurrent collection efficiency across each cell (inset of Fig. 11). This gradient results from the different sheet resistances of the front and back contacts.<sup>25</sup> As the TCO has a higher sheet resistance than the Mo back contact, the photocurrent collection decreases in one direction as the collected current needs to transverse larger distances through the TCO. This effect is very similar to the change of the local voltage one sees in

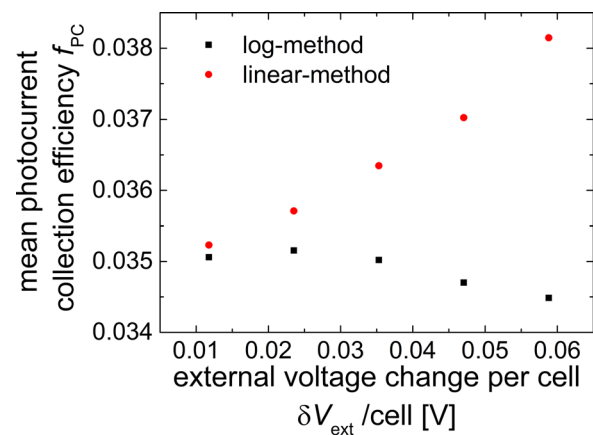


FIG. 10. The photocurrent collection efficiency mean of the whole module determined with the two different calculation methods, depending on  $\delta V_{ext}$ . Red circles: linear-method. Black squares: determination from voltage images with the log-method.

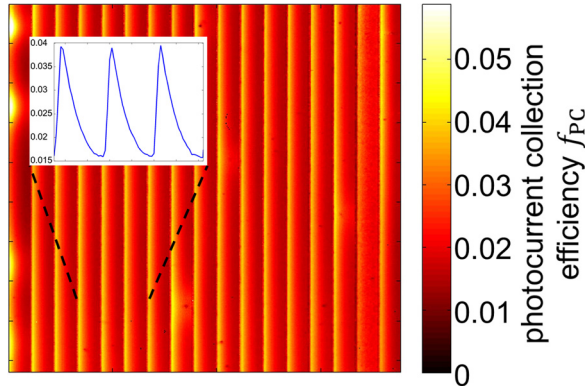


FIG. 11. Photocurrent collection efficiency image of sample 2 at an operating point of 0.68 V/cell.

simple EL images but now we can quantify its influence on the charge carrier collection properties, e.g., under these conditions the probability for additionally generated charge carriers to contribute to the external current is nearly three times lower when they are generated on the right side of the cell as compared to charge carriers generated on the left side of the cell.

### C. Discussion and simulation

It is somewhat counter intuitive that the shunted cell exhibits a larger photocurrent collection efficiency than a non-shunted cell. A shunt in a single cell usually leads to less collected photocurrent as the generated current is lost across the shunt instead of reaching the terminals.<sup>14</sup> This increased photocurrent collection efficiency of the shunted cell in a module results from the series connection of the cells. We can describe the photocurrent collection efficiency of a shunted cell by dividing an additional photocurrent  $\delta I_L^{shc}$  generated in this cell into two parts. One part recombines within the shunted cell, while the other part is collected at the terminals of the module. Mathematically we can describe the part  $\delta I_{ext}$  collected at the terminals as

$$\delta I_{ext} = \frac{\delta I_L^{shc} r_{shc}}{r_{shc} + (n-1)r_{nshc}}, \quad (11)$$

since the resistance of the shunted cell  $r_{shc}$  (which consists of the junction resistance and the shunt resistance) is connected in parallel to the terminals. The resistance to the terminals can be described as  $(n-1) \cdot r_{nshc}$  where  $r_{nshc}$  is the resistance of the non-shunted cells. Note that we use small  $r$  to describe the differential resistances of the cells, which are dependent on their operating point. Rewriting Equation (11) yields

$$\frac{\delta I_{ext}}{\delta I_L^{shc}} = f_{PC} = \frac{1}{1 + \frac{(n-1)r_{nshc}}{r_{shc}}}. \quad (12)$$

Thus,  $f_{PC}$  of the shunted cell mainly depends on the ratio of the differential resistances of the shunted and non-shunted cells. Note that a similar expression was derived in Ref. 12 (Equation (11), therein), which links  $f_{PC}$  and the series

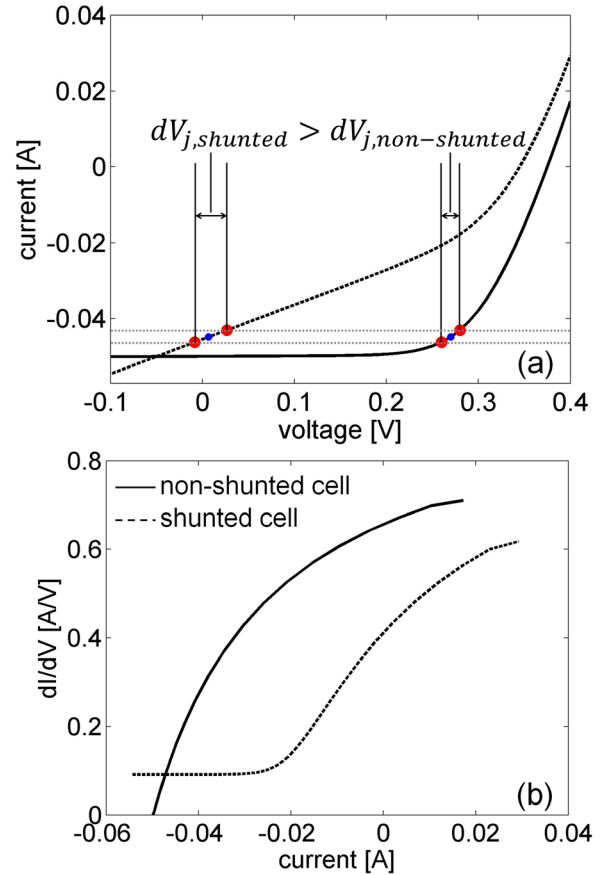


FIG. 12. (a) Exemplary current/voltage characteristics of a shunted (dashed line) and a non-shunted cell (solid lines), determined with the one diode model. (b) Differential conductance of the two  $J/V$  characteristics plotted versus their respective current. The differential conductance is lower for the shunted cell if the current through the cells is only slightly increased. This increases the junction voltage change of the shunted cell  $dV_{j,shunted}$  which again increases its photocurrent collection efficiency.

resistance in cells. In Fig. 12(a), the  $J/V$  characteristics of a shunted and a non-shunted cell determined with a simple arbitrary one diode model is shown. A series connection of the two cells implies that the current through both cells is the same and Fig. 12(a) shows how the same current change through both cells results in a larger voltage change and therefore a larger photocurrent collection efficiency in the shunted cell. Fig. 12(b) shows the differential conductance ( $dI/dV$ ) of these two characteristics plotted versus the current through the cells. At low currents, the shunted cell has the higher differential conductance and above  $-0.048$  A the non-shunted cell shows the higher differential conductance. The shunted cell operates at lower voltages, which means that even at slightly increased currents the differential conductance of the shunted cell is reduced compared to the non-shunted cell. According to Equation (12) and Fig. 12(b) we can therefore identify three main current regions which should lead to different photocurrent collection efficiencies.

- (1) At low currents the  $r_{shc}$  is much lower than  $r_{nshc}$ . From Equation (12) we see that this would lead to a photocurrent collection efficiency of the shunted cell close to zero.
- (2) At increased currents we see that  $r_{shc}$  can be larger than  $r_{nshc}$ . This leads to the result we see in Fig. 9, where the

photocurrent collection efficiency of the shunted cells is larger than that of the non-shunted cells.

- (3) If the current is further increased,  $r_{shc}$  approaches  $r_{nshc}$ , leading to a photocurrent collection efficiency of  $1/n$  in Equation (12). However, note that this equation does not include losses of the photocurrent due to the usual series resistance. Thus, in a realistic case the photocurrent collection efficiency decreases even further and the photocurrent collection efficiency of the shunted cell and the non-shunted cell become equal (compare Fig. 11).

One could also state that the region which experiences the largest voltages change when the current through the module changes is the current limiting part of the module. We therefore see in Fig. 12 that the non-shunted cells limit the current through the module at low currents, while towards higher currents it is the shunted cells. As the photocurrent collection efficiency is determined by the local voltage change when the external voltage (i.e., also the external current) changes it also shows the regions which are limiting the current through the module. Thus, the shunted cells in Fig. 9 show a higher photocurrent collection efficiency as they are limiting the overall current through the module. Changing the illumination of shunted cell has a larger impact on the overall current output of the module compared to changing the illumination of a non-shunted cell.

In the following, we again use network simulations to support our hypothesis that the increase of the photocurrent collection efficiency across the shunted cell results from the series interconnection and can be described with Equation (12). The simulations make it possible to determine the photocurrent collection efficiency also at low working points where measuring it with luminescence is difficult due to the low signal to noise ratio. Additionally, we can compare the determined photocurrent collection efficiencies of cells connected to a module with the determined photocurrent collection efficiency of the same cells without the influence of the series interconnection. For the simulation, we use the model describing the defected module from Section II C.

Fig. 13 shows the simulated collection efficiencies at various operating points. At the low external voltage (4 V, Fig. 13(a)), the non-shunted cells limit the overall current through the module. Zero or even a negative voltage drops across the shunted cell and the photocurrent collection efficiency of the shunted cells is very low as predicted in Equation (12). If the illumination of the shunted cell is slightly changed it would make no difference on the external current. This case could not be reproduced experimentally as the luminescence signal was not measurable at such low operating points. At a higher operating point (9.5 V, Fig. 13(b)), the photocurrent collection efficiency is now higher for the shunted cell than for the other cells. At this operating point, the shunted cells limit the module current. A change of the illumination of the shunted cells would lead to greater change of the external current. Note that this result is qualitatively similar to the experimental result in Fig. 9, which shows that the experimental determination of the photocurrent collection efficiency via luminescence is working well. The quantitative differences indicate that the parameterization of the shunts in the module was not entirely

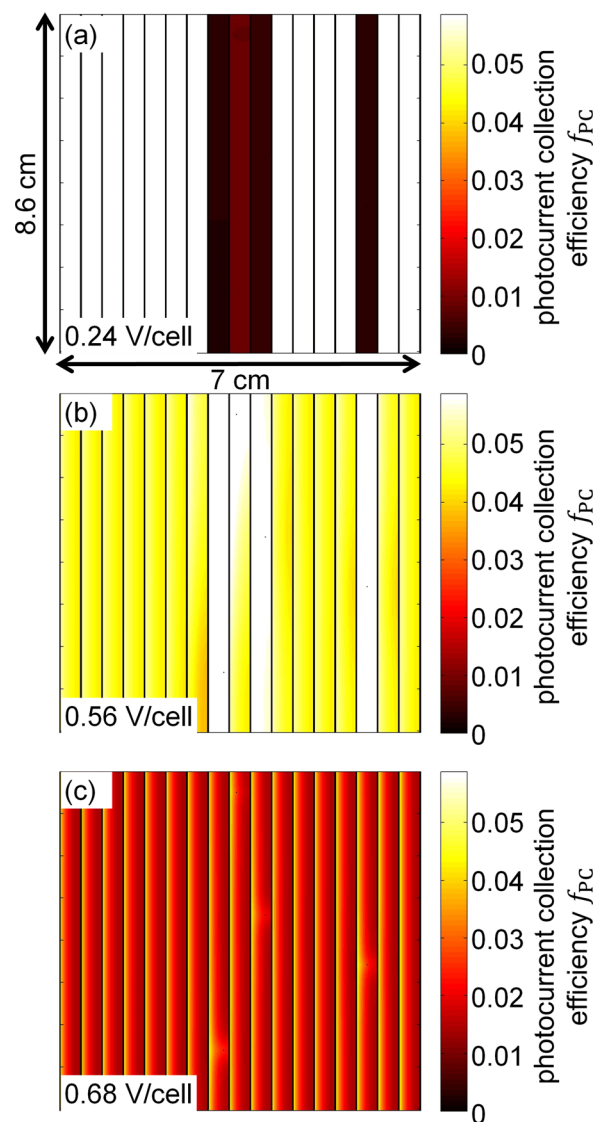


FIG. 13. Simulated photocurrent collection efficiency images of a shunted module. (a) At a terminal voltage of 0.26 V/cell. The shunted cells show a photocurrent collection efficiency of zero as the non-shunted cells limit the overall current. (b) At a terminal voltage of 0.55 V/cell. The shunted cells show higher photocurrent collection efficiencies as they are limiting the overall current through the module. (c) At a terminal voltage of 0.68 V/cell. The shunted cells look very similar to the other cells as the influence of the shunt is reduced.

correct. If the operating point is increased even further to 11.5 V (Fig. 13(c)) the influence of the shunt is reduced, and the photocurrent collection of the shunted cell becomes again similar to the non-shunted cells. This simulation is also very close to the experimentally determined photocurrent collection efficiency in Fig. 11.

To look at the behavior of the shunted cell within the module in more detail, we extracted the individual cell voltages (the operating point of each cell) from our simulation and plotted them versus the operating point of the module (Fig. 14). This figure also shows the corresponding mean photocurrent collection efficiencies of a shunted and non-shunted cell. We clearly see the three voltage regions predicted by Equation (12). At low applied module voltages (below 6 V), we see that the voltage across the shunted cell is negative and



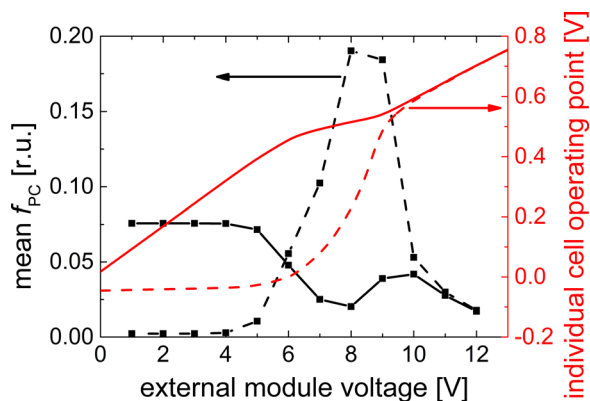


FIG. 14. Dependency of the individual cell voltage (red lines) and the mean photocurrent collection efficiency (black connected squares) of the shunted (dashed line) and a non-shunted cell (solid line) on the externally applied module voltage. The voltage across the non-shunted cell increases linearly with the external module voltage. It differs from this linear behavior between 6 and 9 V as the voltage drop across the shunted cells starts to change. This influence of the shunted cells on the voltage drop across the non-shunted cells results in the dip we see in the photocurrent collection efficiency around the same voltages. Otherwise we would see a monotonous decrease with the external module voltage. The individual cell voltage of the shunted cell is negative in the beginning and shows a non-linear increase with the externally applied voltage. The photocurrent collection of the shunted cell is low at low voltages, shows a maximum around 8.5 V, and decreases again towards higher voltages.

does not change, and the photocurrent collection efficiency of the shunted cell is zero. At higher voltages above 6 V, the applied voltage across the shunted cell changes faster than the voltage across the other cells. The shunted cell becomes current limiting and therefore the photocurrent collection efficiency of the shunted cell (also shown in Fig. 14) increases above the photocurrent collection efficiency of the non-shunted cells. If the external voltage is increased even further, then the change of the voltage across the shunted and non-shunted cells become similar and the photocurrent collection efficiency of the shunted cell decreases again, due to the increasing operating point. Another interesting behavior is the change of the gradient of the voltage curve across the non-shunted cell when voltage starts to drop across the shunted cells. This leads to a dip of the photocurrent collection around 8 V for the non-shunted cells. As the shunted cells are limiting the current around this operating point, illumination changes on the non-shunted cells have very little effect on the external current and in this case, the photocurrent collection efficiency of a non-shunted cells actually rises towards higher operating points.

From the simulation it was also possible to calculate the photocurrent collection efficiencies for each cell individually (by taking the voltages across each individual cell as externally applied voltage) and plot them versus their actual operating point (Fig. 15). Such a measurement is not possible experimentally as the individual cell voltages are not accessible within a module. We see that the influence of the shunt on the individual photocurrent collection efficiencies of the single cells is relatively small compared to the results determined directly from the module. The photocurrent collection efficiencies of the shunted and non-shunted cell decrease with the operating point and do not show a maximum for the

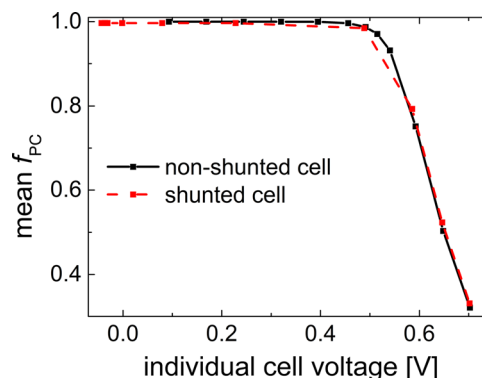


FIG. 15. Mean photocurrent collection efficiency of the non-shunted (red dashed) and shunted cell (black solid) determined individually and plotted versus their real operating point. Determined with the individual voltage changes and operating points accessible from the simulation. Both show the characteristic decrease of the photocurrent collection with the externally applied voltage. The difference of the individual photocurrent collection efficiency between the two cells is relatively small, while it shows a completely different behavior if these two cells are connected in series within a module as shown in Fig. 14.

shunted cell, as it was the case for the complete module measurement. This maximum in Fig. 14 is created by the current-limiting effects which results from the series connection. The photocurrent collection efficiency measurement of the whole module thus does not give information about the performance of the individual cells alone, but rather how they act when combined within a module. While this means that a straightforward interpretation of the  $f_{PC}$  of cells in a module is not possible, it gives useful information about the current limiting regions and how they change at different voltages.

#### IV. CONCLUSION

In this work, we show how both EL and EM-PL images of CIGS solar modules can be used to calculate  $J/V$ -characteristics of individual solar cells within a module, under realistic working conditions. Both methods can be used but one should keep in mind that depending on the sample (sheet resistance, etc.) determining the cell voltage from averaging local junction voltages can be erroneous. The method using EL measurements is less reliable under higher injection conditions due to varying local current flows and the exponential dependence of the local current on the local voltage, while the method using EM-PL is more reliable around the  $V_{oc}$  and less reliable at lower voltages for the same reasons. This is also important if one wants to calibrate luminescence measurements to real voltages. Additionally, this complicates the validation of the reciprocity theorem. Discrepancies as seen in Ref. 11 could at least in part be due to the differences in the local voltage distribution which result from the different injection conditions.

The photocurrent collection efficiency of the cells within the module was calculated, using only the external module voltage and four/three (for the linear/log method, respectively) luminescence images. When comparing the two different methods, we found that the linear approximation method is more influenced by the size of the external voltage

variation, which is a disadvantage at low signal to noise ratios. The error resulting from a large chosen external voltage variation is less severe if the log-method is used. The measured photocurrent collection efficiency for modules cannot be straightforwardly interpreted as a simple figure of merit, as defective cells can show larger or lower photocurrent collection efficiency than the rest of the module, depending on the defect and the working point. This behavior was confirmed by simulations. Instead, the photocurrent collection efficiency of a module has to be interpreted as a factor which describes the influence of a specific region on the collected current of the module.

## ACKNOWLEDGMENTS

This work has been supported by the “OptiCIGS” Project (FKZ 0325724A). Special thanks go to the project partners Raymund Schäffler and Jean-Patrick Theisen (“Manz CIGS Technology”) for providing the samples used in this work.

- <sup>1</sup>T. Fuyuki, H. Kondo, T. Yamazaki, Y. Takahashi, and Y. Uraoka, *Appl. Phys. Lett.* **86**, 262108 (2005).
- <sup>2</sup>T. Trupke, R. A. Bardos, M. C. Schubert, and W. Warta, *Appl. Phys. Lett.* **89**, 044107 (2006).
- <sup>3</sup>K. Bothe and D. Hinken, in *Semiconductors and Semimetals*, Advances in Photovoltaics Vol. 2, edited by G. P. Willeke and E. R. Weber (Academic Press, Burlington, 2013), Vol. 89, p. 259.
- <sup>4</sup>A. Helbig, T. Kirchartz, R. Schaeffler, J. H. Werner, and U. Rau, *Sol. Energy Mater. Sol. Cells* **94**, 979 (2010).
- <sup>5</sup>G. Brown, A. Pudov, B. Cardozo, V. Faifer, E. Bykov, and M. Contreras, *J. Appl. Phys.* **108**, 074516 (2010).

- <sup>6</sup>S. Johnston, T. Unold, I. Repins, R. Sundaramoorthy, K. M. Jones, B. To, N. Call, and R. Ahrenkiel, *J. Vac. Sci. Technol.* **28**, 665 (2010).
- <sup>7</sup>M. Paire, L. Lombez, J.-F. Guillemoles, and D. Lincot, *Thin Solid Films* **519**, 7493 (2011).
- <sup>8</sup>M. Pawlowski, P. Zabierowski, R. Bacewicz, H. Marko, and N. Barreau, *Thin Solid Films* **519**, 7328 (2011).
- <sup>9</sup>A. Gerber, V. Huhn, T. M. H. Tran, M. Sieglösch, Y. Augarten, B. E. Pieters, and U. Rau, *Sol. Energy Mater. Sol. Cells* **135**, 35 (2015).
- <sup>10</sup>B. Misic, B. E. Pieters, J. P. Theisen, A. Gerber, and U. Rau, *Phys. Status Solidi A* **212**, 541 (2015).
- <sup>11</sup>T. C. M. Müller, T. M. H. Tran, B. E. Pieters, A. Gerber, R. Carius, and U. Rau, *Appl. Phys. Lett.* **103**, 183504 (2013).
- <sup>12</sup>J. Wong and M. A. Green, *Phys. Rev. B* **85**, 235205 (2012).
- <sup>13</sup>J. Wong, *IEEE Trans. Electron Devices* **60**, 917 (2013).
- <sup>14</sup>U. Rau, V. Huhn, L. Stoicescu, M. Schneemann, Y. Augarten, A. Gerber, and B. E. Pieters, *Appl. Phys. Lett.* **105**, 163507 (2014).
- <sup>15</sup>U. Rau, *Phys. Rev. B* **76**, 085303 (2007).
- <sup>16</sup>U. Rau, *IEEE J. Photovoltaics* **2**, 169 (2012).
- <sup>17</sup>P. Würfel, T. Trupke, T. Puzzer, E. Schäffer, W. Warta, and S. W. Glunz, *J. Appl. Phys.* **101**, 123110 (2007).
- <sup>18</sup>D. Hinken, C. Schinke, S. Herlufsen, A. Schmidt, K. Bothe, and R. Brendel, *Rev. Sci. Instrum.* **82**, 033706 (2011).
- <sup>19</sup>J. A. Giesecke, M. The, M. Kasemann, and W. Warta, *Prog. Photovoltaics* **17**, 217 (2009).
- <sup>20</sup>T. Kirchartz, A. Helbig, and U. Rau, *Sol. Energy Mater. Sol. Cells* **92**, 1621 (2008).
- <sup>21</sup>M. Glatthaar, J. Haunschild, R. Zeidler, M. Demant, J. Greulich, B. Michl, W. Warta, S. Rein, and R. Preu, *J. Appl. Phys.* **108**, 014501 (2010).
- <sup>22</sup>M. Wolf and H. Rauschenbach, *Adv. Energy Convers.* **3**, 455 (1963).
- <sup>23</sup>B. E. Pieters, in *Photovoltaic Specialist Conference (PVSC), 2014 IEEE 40th*, Denver, CO, 8–13 June 2014 (IEEE, 2014), p. 1370.
- <sup>24</sup>U. Rau and T. Kirchartz, in *Photon Management in Solar Cell*, edited by R. B. Wehrspohn, U. Rau, and A. Gombert (Wiley-VCH, Weinheim, 2015), p. 21.
- <sup>25</sup>T. M. H. Tran, B. E. Pieters, C. Ulbrich, A. Gerber, T. Kirchartz, and U. Rau, *Thin Solid Films* **535**, 307 (2013).